Environ. Sci. Technol. **XXXX,** *xxx,* 000–000

Sites of Lu(III) Sorbed to and Coprecipitated with Hectorite

NICOLAS FINCK,*,†,§
MICHEL L. SCHLEGEL,‡ AND
DIRK BOSBACH§,||

Institut für Nukleare Entsorgung (INE), Forschungszentrum Karlsruhe, P.O. Box 3640, D-76021 Karlsruhe, Germany, CEA Saclay - DEN/DPC/SCP/LRSI, P.O. Box 11, F-91191 Gif-sur-Yvette, France, Institut für Energieforschung 6, Forschungszentrum Jülich, D-52425 Jülich, Germany, and Helmholtz Virtual Institute "Advanced Solid-Aqueous RadioGeochemistry", Germany

Received July 1, 2009. Revised manuscript received October 9, 2009. Accepted October 14, 2009.

The Lu(III) binding mechanisms by trioctahedral smectite hectorite in aqueous systems were investigated by extended X-ray absorption fine structure (EXAFS) spectroscopy. Coprecipitated hectorite (Lu755Hec), its precursor phase (Lu/Brucite), and the surface sorbed hectorite (Lu/SHCa1) were prepared as oriented samples to collect polarized EXAFS (P-EXAFS) data. EXAFS analysis indicated that Lu(III) is 6-fold coordinated by oxygen in Lu/Brucite and in Lu755Hec, and surrounded by Mg/Si shells. The angular dependence of the O and Mg coordination numbers for Lu/Brucite hinted an Lu(III) incorporation in brucite layers. Mg and Si cationic shells were detected at distances suggesting a clay-like octahedral environment in Lu755Hec. EXAFS data for Lu/SHCa1 were consistent with Lu(III) forming inner-sphere surface complexes at hectorite platelets edges, but slightly above/below the octahedral plane. Finally, Lu(III) polyhedra share edges(s) and corner(s) with Si tetrahedra upon sorption to silica (Lu/Silica). Lu(III) binding to silicate oligomers or to silicate groups of the clay basal planes and formation of Lu(III) surface complexes during the coprecipitation experiment are marginal.

Introduction

Clay minerals can be major sorbing solids in geological and engineered barriers of high-level nuclear waste (HLW) repositories, depending on the repository concept. They may also form as secondary phases upon alteration of the HLW matrix in the presence of groundwater (*1*). For example, the magnesian smectite hectorite ($Na_{0.33}[Li_{0.33}Mg_{2.67}Si_4O_{10}(OH)_2]$) is frequently observed in HLW glass alteration experiments (*2*). The precipitation of such clay phases can lead to a significant retention of long-lived and radiotoxic radionuclides (RN), including actinides (An) (*3*), as clays are known to retain cations in aqueous systems via a variety of molecular-level binding mechanisms. Specifically, RN may be retained by formation of surface complexes, but also by incorporation into the bulk structure of clay minerals by coprecipitation, resulting in long-term immobilization, especially if a (meta)-stable solid solution forms.

The retention of trace elements by clay minerals is controlled by their formal valence and ionic charge, which also depends on the physicochemical conditions in natural systems. Under reducing conditions, Am, Cm, and some of Pu may occur as trivalent cations. In 6-fold coordination by oxygen, the ionic radii of these trivalent actinides (r^{VI}) (r^{VI}(Am(III)) = 0.98 Å; r^{VI}(Cm(III)) = 0.97 Å, r^{VI}(Pu(III)) = 1.00 Å (*4*)), and of their nonradioactive chemical surrogates (*5*) the lanthanides (r^{VI}(Ln(III)) > 0.86 Å), are somewhat larger than that of major cations of clay octahedral sheets (e.g., r^{VI}(Mg(II)) = 0.72 Å, r^{VI}(Li(I)) = 0.76 Å, r^{VI}(Fe(II)) = 0.78 Å). However, the difference cannot preclude some incorporation of Ln(III) and An(III) in octahedral sites but the substitution may be hindered by large structural strains (*6*). For example, investigations (*7*) on Cu, Zn, Cd, and Pb coprecipitated with hectorite showed that the smaller Cu (r^{VI}(Cu(II)) = 0.73 Å) and Zn (r^{VI}(Zn(II)) = 0.74 Å) were more easily incorporated in clay octahedral sites than the larger Cd (r^{VI}(Cd(II)) = 0.95 Å) and Pb (r^{VI}(Pb(II)) = 1.14 Å). Recently, time-resolved laser fluorescence spectroscopy data collected for Eu(III) (r^{VI}(Eu(III)) = 0.95 Å) and Cm(III) coprecipitated hectorite (*8, 9*) indicated that the heavy ions were located in bulk solids. Data were consistent with Ln/An present in octahedral sites from the early stage multistep synthesis protocol, but no definite proof could be given. Therefore, the reality of a Ln(III) or An(III) incorporation in the clay octahedral sheet should be demonstrated.

In the present study, the Lu(III) uptake site by coprecipitation with and by sorption on hectorite was deciphered by extended X-ray absorption fine structure (EXAFS) spectroscopy. Powder EXAFS spectroscopy provides a spectroscopic signature of the molecular environment of X-ray absorbing atoms, hence it readily discriminates distinct sorption mechanisms. However, powder EXAFS analysis for absorbing atoms located in the clay octahedral sheets may be tricky, as these atoms are surrounded by neighboring cations located in the octahedral layer (R ~3.05−3.10 Å) and in the tetrahedral layer (R ~3.20−3.25 Å). The EXAFS contributions of these shells may overlap, complicating the structural analysis of the crystallochemical environments. However, these distinct shells may be singled out by polarized EXAFS (P-EXAFS) spectroscopy, as amply demonstrated for metal cations sorbed on hectorite (*10*). The contribution from cations in the tetrahedral sheet is minimized when the experimental angle (α) between the hectorite layer plane and the electric field vector of the X-ray beam equals 0°, and enhanced at α = 90° (*11*). The opposite angular dependence is observed for cations located in the octahedral sheet. Thus, the dissimilarities in molecular environments of Lu(III) either sorbed on, or coprecipitated with, hectorite could be revealed using P-EXAFS spectroscopy. These results demonstrate for the first time that large Lu(III) can be incorporated in the clay octahedral sheet.

Experimental Section

Sample Preparation. All solutions were prepared with Milli-Q water (18 M·cm^{-1}) and reactants of ACS or higher grade. A Lu(III) (0.08 M) stock solution was prepared by dissolving Lu_2O_3 in 2% perchloric acid. Hectorite was coprecipitated (*12*) in the presence of Lu(III) (sample Lu755Hec). Briefly, a Lu(III)-containing brucite precursor (Mg:Lu molar ratio of 755:1) was freshly precipitated and washed 4 times with Milli-Q water. The resulting slurry was refluxed (100 °C) under constant stirring in the presence of LiF. After 30 min, a silica

* Corresponding author phone: +49 (0) 7247-82-4321; e-mail: Nicolas.finck@ine.fzk.de.
† Institut für Nukleare Entsorgung.
‡ CEA Saclay.
§ Institut für Energieforschung.
|| Helmholtz Virtual Institute.

sol (Ludox HS-30, Aldrich) was added and the suspension reacted for additional 48 h. Any remaining precursor phase (brucite) was removed by washing the resulting hectorite with HCl (pH 3). A Lu(III)-containing brucite (Mg:Lu molar ratio of 290:1; sample Lu/Brucite) was also freshly precipitated and washed several times with Milli-Q water, and used as a reference compound. Lu(III) was sorbed on hectorite (sample Lu/SHCa1) by contacting the aqua ions with the <2 μm fraction of the reference clay mineral hectorite SHCa-1 (Source Clay Repository) ([Lu] = 90 μM, 2 g/L hectorite, pH 7.3, 0.5 M $NaClO_4$). Details on the clay purification and characterization can be found elsewhere (*13*). Finally, Lu(III) aquo ions were sorbed on silica sol ([Lu] = 1.7 mM, 38 g/L silica, pH 7.5, no background electrolyte; sample Lu/Silica) for 72 h under a nitrogen atmosphere. This last reference is expected to mimic the environment of Lu(III) bound to silica groups, either on hectorite basal planes, or to any amorphous silica phase left from the clay synthesis.

Lu755Hec and Lu/Brucite were characterized by X-ray diffraction (XRD) (Bruker D8 Advance, Cu Kα) and attenuated total reflectance−Fourier transform infrared (ATR−FTIR) spectroscopy (Bruker IFS 55) prior to EXAFS experiments. Self-standing films were prepared by slow filtration of Lu/Brucite, Lu/SHCa1, and Lu755Hec suspensions on cellulose nitrate filters (0.025 μm, Millipore). This protocol readily provided highly textured self-supporting films to perform P-EXAFS experiments. The Lu/silica suspension was filtered to obtain a dry pellet for powder EXAFS characterization. The precipitation of $Lu(OH)_3$(s) during the sorption experiments was ruled out based on thermodynamic considerations (*14*) for Lu/SHCa1 and by the absence of the characteristic absorption bands (3330 and 3210 cm^{-1}) (*15*) on the infrared spectrum collected for the Lu/silica filtered suspension.

EXAFS Spectroscopy. Lutetium L_{III}-edge (9.244 keV) EXAFS spectra were collected on the FAME beamline (*14*) of the ESRF (Grenoble, France) with a storage ring energy of 6 GeV and a ring current of ~200 mA. Energy calibration was done by setting the K-edge of a Cu foil at 8.979 keV. All spectra were collected in fluorescence-yield detection mode using a 30-element Ge solid-state detector (Canberra). Powder EXAFS spectra were collected for the Lu(III) stock solution (sample $Lu(III)_{aq}$) and for Lu/silica. P-EXAFS spectra were recorded at angles α = 35, 55, and 80° for all films, and at α = 10° for Lu/brucite and Lu755Hec. The spectrum at 10° for Lu/SHCa1 was extrapolated from spectra collected at higher angles (*13*).

Analysis of the EXAFS data was performed following standard procedures by using Athena and Artemis interfaces to the Ifeffit software (*17*). The EXAFS spectra were apodized with a Kaiser-Bessel window and Fourier transformed. The Fourier transform (FT) envelopes display amplitude maxima or peaks at apparent distances ($R + \Delta R$) that differ from half the length of the scattering path (R equals the absorber − backscatter distance for single scattering) by ~ −0.3 Å because of phase shift of the EXAFS waves (*18*). Data fit was performed in R-space using phase and amplitude functions calculated with fefff8 (*19*). The amplitude reduction factor (S_0^2) was set to 1.0 to correctly reproduce the number of Lu(III) neighboring O atoms in water, in agreement with previous studies (*20, 21*). For a given film, the data were fit simultaneously at all angles, using a single value for ΔE (edge-shift between theoretical and experimental data), and for a given shell, a common bond length and Debye−Waller factor (accounting for static and thermal disorder) (*10*) at all angles. The fit quality was quantified by the R_f factor (*22*). The experimental uncertainty on α in the P-EXAFS measurements is estimated to ±1° or less. The uncertainty on the EXAFS-derived structural distances is estimated to ±0.02 Å and the precision on the number of neighboring atoms to ±20%. Note that Mg (Z = 12) and Si (Z = 14) cannot be discriminated solely by the phase and amplitude of their EXAFS contribution. However, the differences in Mg and Si coordination (6-fold vs 4-fold) and in Mg−O and in Si−O interatomic distances add constraints on the nature of the backscattering shells for sorbed cations.

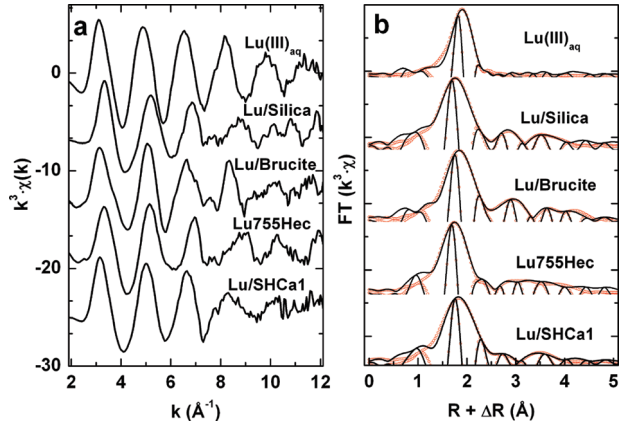

FIGURE 1. (a) k^3-weighted Lu L_{III}-edge EXAFS spectra for Lu(III) in solution ($Lu(III)_{aq}$), Lu(III) sorbed on silica sol (Lu/silica), Lu-containing precursor (Lu/brucite) at α = 35°, Lu(III) coprecipitated with hectorite (Lu755Hec) at α = 35°, and Lu(III) sorbed on hectorite (Lu/SHCa1) at α = 35°. (b) Experimental (solid lines) and simulated (dotted lines) amplitudes and imaginary parts of the Fourier transforms.

Results and Interpretation

X-ray Diffraction and Infrared Spectroscopy. The infrared spectra collected for Lu/brucite and for freshly precipitated brucite were identical (Figure S1 in Supporting Information (SI)). The sharp band at ~3695 cm^{-1} corresponds to the hydroxyl stretching frequency (*23*) thus clearly identifying the main phase as brucite in Lu/brucite. The Lu755Hec solid phase was identified as hectorite (Figure S1 in SI) from the characteristic absorption bands (*24*) displayed in the spectrum: −OH stretching (~3675 cm^{-1}) and deformation (~651 cm^{-1}) bands of the Mg_3OH units, and Si−O stretching (~987 and ~694 cm^{-1}) bands. Residual amorphous silica was also observed (~795 and ~1125 cm^{-1}) (*25*), but none of the spectra displayed the characteristic −OH absorption bands for $Lu(OH)_3$(s) (3330 and 3210 cm^{-1}) (*15*). The X-ray diffractogram for Lu/brucite (Figure S2) matched the XRD pattern expected for brucite (*26*). The XRD pattern for Lu755Hec (Figure S2) exhibited a peak at 13.4 ± 0.2 Å that is consistent with a d_{001} basal spacing characteristic of natural and pure synthetic hectorite (*7, 12, 27*).

The presence of Lu(III) led to no significant modification either in the infrared spectra, or on the XRD patterns, confirming its presence in trace amount and dispersed within the matrices. Consequently, the presence of Lu(III) did not significantly influence the hectorite formation or degree of crystallinity. This corroborates previous investigations on the small impact of heavy metal cations (Cd, Cu, Pb, Zn) at trace concentration on the hectorite structure (*7*).

EXAFS Spectroscopy. The EXAFS spectrum for $Lu(III)_{aq}$ displays a single wave frequency with monotonically decreasing amplitude for k > 3 $Å^{-1}$ (Figure 1), consistent with the presence of a single ordered coordination shell of water oxygens. This interpretation is confirmed by the presence of a single major peak at ~1.8 Å on the FT. Only very weak contributions can be observed for higher distances arising either from multiple scattering (MS) within the first coordination sphere, or from single scattering paths from next hydration spheres. The spectrum could be correctly modeled assuming a number of oxygens N_O = 8.0(1.6) at a Lu−O

TABLE 1. Quantitative EXAFS Analysis for the First FT Peak for All Samples[a,b]

				O1 shell			O2 shell				
sample	α	FT range (Å^{-1})	fit range (Å)[c]	R_{Lu-O1} (Å)	N_{O1}	σ^2(Å^2)	R_{Lu-O2} (Å)	N_{O2}	σ^2 (Å^2)	ΔE_0[d] (eV)	R_f[e]
Lu/SHCa1	10°	3.7 − 9.4	1.5 − 4.2	2.19(2)	2.8(2)	0.005[f]	2.33(2)	4.0(2)	0.005[f]	4.1(2)	0.004
	35°				2.7(1)			4.2(1)			0.002
	55°				2.6(1)			4.3(1)			0.003
	80°				2.5(1)			4.6(1)			0.002
Lu755Hec	10°	3.9 − 9.8	1.5 − 4.2	2.19(1)	5.4(3)	0.010				1.9(6)	0.014
	35°				5.5(3)						0.008
	55°				5.6(4)						0.011
	80°				5.5(2)						0.014
Lu/brucite	10°	3.8 − 9.6	1.6 − 4.3	2.26(2)	6.5(1.3)	0.010				3.5(2)	0.006
	35°				6.1(1.2)						0.004
	55°				5.6(2)						0.006
	80°				5.3(1.1)						0.009
Lu/silica	35°	3.9 − 9.0	1.5 − 4.2	2.22(1)	5.5(1.1)	0.011				3.9(1.1)	0.008
$Lu(III)_{aq}$	35°	3.8 − 12.5	1.7 − 2.3	2.31(2)	8.0(1.6)	0.008				3.9(2.4)	0.0008

[a] The data were fit over the entire fit range considering all shells from Table 1 and 2 for the films and Lu/silica. [b] Number in parentheses at the end of value indicates the uncertainty. [c] $R + \Delta R$ interval for the fit. [d] Threshold energy E_0 taken as zero crossing of the second derivative. [e] Figure of merit of the fit (*20*). [f] Values coupled during the fitting procedure.

TABLE 2. Quantitative EXAFS Analysis of Higher Atomic Shells[a,b,c]

Lu/silica

α	R_{Lu-Si1}(Å)	N_{Si1}	σ^2 (Å^2)	R_{Lu-Si2}(Å)	N_{Si2}	σ^2 (Å^2)	R_{Lu-Si3}(Å)	N_{Si3}	σ^2 (Å^2)	R_{Lu-O2}(Å)	N_{O2}	σ^2 (Å^2)
35°	3.04(2)	0.8(2)	0.009	3.50(2)	1.6(3)	0.009	3.77(2)	1.5(7)	0.009	4.12(2)	3.1(1.2)	0.009

Lu755Hec

α	R_{Lu-Mg} (Å)	N_{Mg}	σ^2 (Å^2)	R_{Lu-Si2}(Å)	N_{Si2}	σ^2 (Å^2)	R_{Lu-Si3}(Å)	N_{Si3}	σ^2 (Å^2)	R_{Lu-Si4}(Å)	N_{Si4}	σ^2 (Å^2)
10°	3.12(2)	0.5(1)	0.008	3.35(2)	0.9(4)	0.008	3.82(2)	1.4(3)	0.008	4.35(2)	2.0(8)	0.008
35°		0.9(2)			1.3(3)			1.2(5)			1.9(7)	
55°		1.4(3)			1.5(5)			0.9(7)			1.9(1.0)	
80°		1.9(4)			2.0(3)			0.5(5)			2.3(6)	

Lu/Brucite

α	R_{Lu-Mg} (Å)	N_{Mg}	σ^2 (Å^2)	R_{Lu-O2}(Å)	N_{O2}	σ^2 (Å^2)	R_{Lu-O3}(Å)	N_{O3}	σ^2 (Å^2)
10°	3.29(1)	2.2(4)	0.005	4.18(2)	5.1(1.7)	0.009	4.52(2)	5.2(2.1)	0.009
35°		1.9(4)			5.1(1.8)			5.3(2.2)	
55°		1.7(3)			4.7(1.5)			4.1(1.7)	
80°		1.4(3)			3.9(1.5)			3.0(1.8)	

Lu/SHCa1

α	R_{Lu-Mg}(Å)	N_{Mg}	σ^2 (Å^2)	R_{Lu-Si2}(Å)	N_{Si2}	σ^2 (Å^2)	R_{Lu-Si3}(Å)	N_{Si3}	σ^2 (Å^2)
10°	3.16(2)	3.0(6)	0.005	3.33(1)	2.2(4)	0.005	3.95(1)	1.5(4)	0.007
35°		2.8(4)			2.0(4)			1.6(3)	
55°		2.8(6)			1.8(1)			2.1(2)	
80°		2.6(2)			1.5(3)			2.0(3)	

[a] The data were fit over the entire fit range considering all shells from Table 1 and 2 for the films and Lu/silica. [b] A C shell was considered to fit the data for Lu755Hec ($N_C = 0.6(1)$, $R_{Lu-C} = 2.88(2)$, $\sigma^2 = 0.008$ Å^2) and Lu/brucite ($N_C = 1.1(2)$, $R_{Lu-C} = 2.84(1)$, $\sigma^2 = 0.005$ Å^2). [c] Number in parentheses at the end of value indicates the uncertainty.

distance $R_{Lu-O} = 2.31(2)$ Å (Table 1). These results compare well with reported distances and coordination numbers (*20, 28*).

The EXAFS spectrum for Lu/silica has distinct nodes, e.g., at $k \sim 7.5$ and ~ 9.5 Å^{-1}, which are absent from $Lu(III)_{aq}$ (Figure 1), and therefore cannot be attributed only to MS within the first coordination sphere. Instead, they can be attributed to next-nearest shells. Indeed, the FT displays a peak at ~1.8 Å originating from the oxygen coordination sphere and additional contributions at ~2.9 and ~3.6 Å that may be related to the presence of next-nearest Si and/or O neighbors. Furthermore, these more distant peaks are slightly asymmetric, suggesting the presence of more than two next-nearest shells. The first FT peak was well modeled by a shell of 5.5(1.1) O atoms at $R_{Lu-O1} = 2.22(1)$ Å (Table 1). Both N_{O1} and R_{Lu-O1} are consistent with Lu(III) 6-fold coordinated by O (*4*). The next-nearest contribution was modeled assuming Si shells located at 3.04(2) and 3.50(2) Å. Finally, the FT peak at ~3.6 Å could be adequately fitted by combining a Si ($R_{Lu-Si3} = 3.77(2)$ Å) and a possible O ($R_{Lu-O2} = 4.12(2)$ Å) shell.

The EXAFS data indicate that Lu is bound to a solid silica phase. The ~6 O in the Lu first coordination sphere compare well with data reported for Yb-, Er-, Dy-, and La-bearing silicate glasses (*29*−*31*) and for Cm-bearing borosilicate glass (*32*). The Si detected as next neighbors in Lu/silica correspond to silica units, possibly binding the Lu polyhedra by sharing edge(s) and corners (R_{O-Si} = 1.64 Å) (*31*), with geometries ranging from aligned to bent. The first Lu−Si distance is short (R_{Lu-Si1} = 3.04(2) Å) and may only be explained by Si tetrahedra sharing edges with Lu polyhedra. The longer R_{Lu-Si3} = 3.77(2) Å is slightly smaller than the upper limit on Lu−Si distance obtained for Lu and Si polyhedra sharing corners and in an aligned geometry ($R_{Lu-O} + R_{O-Si}$ = 2.22 + 1.64 = 3.86 Å). This binding mode may account for R_{Lu-Si3} by slightly tilting the Si tetrahedron. Finally, the Lu−Si distance of 3.50(2) Å is close to the value reported for Dy-doped silicate glasses (R_{Dy-Si} = 3.60 Å) (*31*), and to the value expected for corner sharing in a bent geometry. Important cancellation effects may arise in the vicinity of Lu from these various geometries and lead to low numbers of detected backscatterers.

The EXAFS spectra collected at α = 35° (powder and polarized EXAFS data are identical at this angle) for Lu/brucite, Lu755Hec, and Lu/SHCa1 all display distinct frequencies (Figure 1), especially at high *k* (e.g., ~7.5 Å^{-1}). As for Lu/silica, these features can be related to the presence of several cationic shells, since MS paths have no large amplitude at high *k*. These spectra are all distinct from each other, e.g., in the [6.5−10 Å^{-1}] range, which points to distinct crystallochemical environments, and possibly distinct cationic shells. All FTs display a first peak originating from O coordinated to Lu. The Lu−O distances obtained by fitting (Table 2) vary between 2.19(2) Å in Lu755Hec and Lu/SHCa1 and 2.33(2) Å in Lu/SHCa1. The short distance is characteristic of 5- to 6-fold coordination, and the longer is characteristic of 7- to 8-fold coordination (*4*). This is in agreement with N_O values from EXAFS analysis (Table 2). A beating node is present on the inverse FT of the Lu/SHCa1 first peak, hinting a split of this shell in two subshells, contrary to Lu/brucite and Lu755Hec. The spectral modeling indicated the presence of ~3 (N_{O1}) and 4−5 O (N_{O2}) backscatterers at 2.19(2) and 2.33(2) Å, respectively. This split is typical of cations sorbed on solid phases (*10*), with some O atoms belonging to bound water molecules (N_{O2}) and some belonging to the sorbent surface (N_{O1}). Additionally, N_{O2} is typical for the hydration shell of Ln(III) forming inner-sphere surface complexes (*33*) at a Lu−O distance characteristic for $Lu(III)_{aq}$ ions.

All FTs display additional contributions at higher distances originating from the presence of next-nearest atomic shells. Only Mg and Si shells were considered to fit well the Lu755Hec and Lu/SHCa1 spectra. In contrast, O shells were used beyond the nearest Mg shell for Lu/brucite. The type of neighbors and the distance from the absorbing atom vary from sample to sample (Table 2), corroborating the presence of distinct crystallochemical environments. The fits were also improved by addition of a C shell for Lu/brucite (~1 atom at R_{Lu-C} = 2.84(1) Å) and Lu755Hec (<1 atom at R_{Lu-C} = 2.88(2) Å). The physical origin of this shell is unclear, but it may correspond to the formation of carbonate species at the high pH during the synthesis. Finally, no neighboring Lu atom was detected in any compound, thus precluding the precipitation of $Lu(OH)_3(s)$.

Small but significant angular dependences can be observed on all sets of P-EXAFS spectra (Figure 2a). The variation in amplitude and sometimes position of the oscillation maxima with α (e.g., ~4 and ~5 Å^{-1}) indicates an anisotropic Lu binding environment in each sample. These oscillation shifts indicate the presence of multiple atomic shells with distinct orientations, meaning that the atoms are structurally bound to the mineral phases. Besides, these spectral dichroisms confirm the texture quality of all self-standing films.

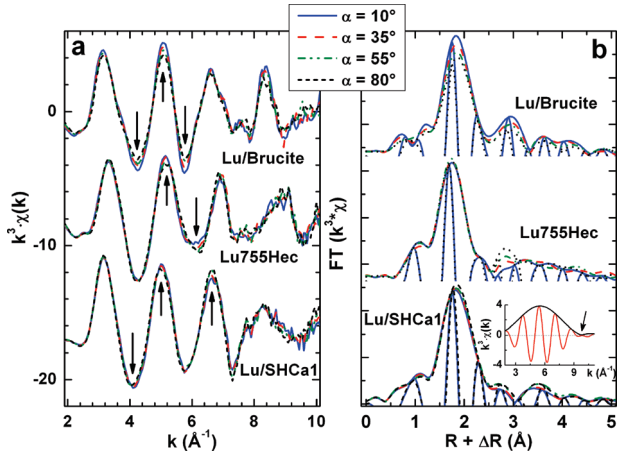

FIGURE 2. (a) Polarized EXAFS spectra for the Lu-containing precursor (Lu/brucite), Lu(III) coprecipitated hectorite (Lu755Hec), and Lu(III) sorbed on hectorite (Lu/SHCa1). (b) Amplitudes and imaginary parts of the Fourier transforms. Insert shows the first peak inverse FT for Lu/SHCa1 at α = 35°.

The amplitude of the Lu/brucite FT peaks near ~1.8 Å (O shell) and ~3.0 Å (Mg shell) decreases with increasing α (Figure 2b), supporting an anisotropic environment around Lu. Back-Fourier transforms of the second FT peak contain isosbestic points (Figure S3), for which the EXAFS oscillations are independent of α. These points are much sensitive to defaults in spectral normalization and their observation attests for the reliability of the data analysis. The octahedral environment suggested from the O shell EXAFS analysis, together with the decrease in O and Mg coordination numbers with increasing α, strongly suggest a Lu incorporation in brucite layers. Additionally, this decrease in number of detected Mg backscatterers with increasing α values (Table 2) hints an in-plane orientation of the Mg neighbors.

Whereas the amplitude of the Lu755Hec first FT peak is almost unaffected by the variation of α (Figure 2b), the amplitude of the peak at $R + \Delta R$ ~2.8 Å increases and its amplitude maximum is shifted to greater distances, suggesting the presence of two overlapped contributions (*11*). A broad feature is present at higher distances and is almost unaffected by α variations. An overlap of several next-nearest shells, e.g., Mg/Si_1 and Mg/Si_2, may account for this FT contribution. The dichroism is obvious as indicated by the back-Fourier transforms of this broad feature, which also contain isosbestic points (Figure S3). Data modeling confirmed a nearly spherical distribution of the O atoms ligated to Lu, as hinted by the absence of N_O angular dependence (Table 1). In contrast, $N_{Mg/Si1}$, and to a lower extent $N_{Mg/Si2}$, displayed clear angular dependences, pointing to a local anisotropic environment around Lu. Finally, the broad feature at higher distances was successfully fitted with Si shells (R_{Lu-Si3} = 3.80(2) Å and R_{Lu-Si4} = 4.35(2) Å).

The amplitude of the Lu/SHCa1 FT peak near ~1.8 Å increases and its amplitude maximum is shifted to greater distances with α (Figure 2b), corroborating the presence of different backscatterers (*11*), i.e., a split in two O subshells. Additional contributions originating from nearest cationic shells can be observed at ~2.9 and ~3.5 Å: these were modeled considering Mg/Si neighbors at 3.16(2) Å and 3.33(1) Å, and a possible Si shell located at 3.95(2) Å. The reliability of the data analysis is again attested from the back-Fourier transforms (Figure S3). The Lu(III) environment in Lu/SHCa1 is significantly different from that of Lu755Hec, which is also different from that of Lu/brucite. None of these samples showed evidence for Lu bound to a solid silica phase (Lu/silica).

Discussion

The multistep synthesis protocol resulted in Lu(III) being sequentially occluded in several distinct environments from the brucite precursor to the fully crystallized clay phase (*8, 9*). In the precursor, the Lu coordination sphere is made by a single O shell and the spectral simulations pointed to a brucite-like octahedral environment. Additional information can be derived from the EXAFS-derived interatomic distances and the knowledge of the brucite structure. Brucite ($Mg(OH)_2$) is made up of $Mg-O_6$ octahedra (R_{Mg-O} = 2.10 Å) sharing O−O edges (R_{O-O} = 2.78 Å, R_{Mg-Mg} = 3.14 Å) (*34*). The simplest hypothesis is to assume that Lu substitutes for Mg in the brucite octahedral sheet, the Lu octahedra sharing O−O edges with Mg octahedra. The EXAFS-derived Lu−Mg distance may thus be obtained by replacing Mg by Lu and summing up the distances from Mg and from Lu to the middle of the shared edge, keeping identical R_{O-O}. The distance between Lu and the shared edge equals: $\sqrt{(2.26^2 - (2.78/2)^2)} = 1.78$ Å. Consequently, the calculated Lu−Mg distance equals (3.14/2) + 1.78 = 3.35 Å, only slightly longer than the experimental distance. Additionally, the increase between R_{Mg-Mg} in brucite (3.14 Å) (*34*) and R_{Lu-Mg} in Lu/brucite (3.29(1) Å) approximately matches the increase in ionic radii (r^{VI}(Mg(II)) = 0.72 Å, r^{VI}(Lu(III)) = 0.86 Å) (*4*). These considerations imply that Lu substitutes for Mg at the octahedral site.

An important structural change from the starting precursor to the crystallized clay mineral is the reduction of the Mg−Mg interatomic distance from 3.14 Å in brucite (*34*) to 3.04 Å in hectorite (*35*). Due to its large ionic radius, Lu(III) should have a limited structural compatibility for clay octahedral sites and local structural deformation and/or a release of Lu(III) to the supernatant (*9*) upon clay formation may be expected. Yet, the presence of significant residual fraction of Lu/brucite precursor or of surface-sorbed or aqueous Lu(III) can be ruled out, as these species would have resulted in a second O shell at $R \geq 2.26(2)$ Å. The obvious dissimilarities in EXAFS spectra among Lu755Hec, Lu/silica, and Lu/SHCa1 also rule out compelling Lu(III) adsorption on the hectorite surfaces, or on any remaining amorphous silica. The detection of Mg and Si as next-nearest neighbors indicates that Lu(III) is structurally associated with hectorite, and the angular dependence on $N_{Mg/Si1}$ and $N_{Mg/Si2}$ further highlights the local anisotropic environment. An incorporation in the hectorite tetrahedral layer can be clearly ruled out owing to size mismatch, and thus Lu(III) may be located in clay octahedral sites.

The simplest hypothesis is to assume that Lu substitutes for Mg and is located at the center of an octahedron (R_{Lu-O} = 2.19(1) Å) sharing O−O edges with Mg octahedra (R_{Mg-O} = 2.08 Å (*35*)). The expected Lu−Mg distance may be obtained by replacing Mg by Lu and summing up the distances from Mg and from Lu to the middle of the shared edge, keeping identical R_{O-O}. The length of the O−O edge shared between Mg octahedra equals $R_{O-O} = 2 \times \sqrt{(2.08^2 - (3.04/2)^2)} = 2.84$ Å. The distance between Lu and the shared edge then equals $\sqrt{(2.19^2 - 1.42^2)} = 1.67$ Å. Consequently, R_{Lu-Mg} = 1.52 + 1.67 = 3.19 Å, only slightly longer than the experimental distance. The small difference can be easily accounted for by some structural relaxation around Lu, possibly involving Lu shift from the center of the octahedral sheet. The Si tetrahedra may then be moved away from their regular position, resulting in R_{Lu-Si2} (Lu755Hec) longer than R_{Mg-Si} (hectorite). However, in that case 6 in-plane Mg and 4 out-of-plane Si (*35*) would be expected to surround Lu, far more than actually obtained from EXAFS simulations. Actually, Li(I) may be coincorporated with Lu(III) in adjacent octahedral sites for local charge compensation. As Li is too light to be detected by EXAFS spectroscopy, this co-incorporation may also account for the small number of detected neighboring Mg. Also, Lu incorporation would be met with significant structural strain around Lu, and this structural disorder would ultimately reduce the number of detected Mg and Si neighbors, consistent with observations.

The presence of Lu(III) at clay octahedral sites may result either from structural incorporation during crystal growth, or from diffusion into octahedral vacancies. However, lanthanide diffusion to vacant octahedral sites may occur only at relatively high temperatures, due to their large hydration energies (*36, 37*). Hence, Lu(III) very likely substitutes for cations at octahedral position in brucite and remains in the layer during hectorite crystallization.

Polarized-EXAFS data indicated that Lu(III) remains hydrated upon sorption on hectorite (Lu/SHCa1), with Lu−O distances (R_{Lu-O1} = 2.33(2) Å) typical of solvated cations, meaning that Lu did not diffuse into clay octahedral sites. However, the presence of Mg and Si cationic shells and their anisotropic distribution rule out the formation of outer-sphere surface complexes. By reference to Lu/Silica, Lu(III) binding to Si oligomers or to silanol groups of the hectorite silica sheet can also be dismissed. Consequently, the formation of inner-sphere surface complexes near surface-exposed Mg appears as the only plausible Lu retention mechanism. Because Mg octahedra are only exposed at hectorite edges, Lu(III) can only be retained at these layer edges.

Additional constraints on the nature of the Lu(III) surface complexes can be derived from the absence of angular dependence on $N_{Mg/Si1}$ and from the preferential in-plane orientation of the Mg/Si_2 shell. A spherical Mg distribution around Lu might account for the absence of $N_{Mg/Si1}$ angular dependence. However, a spherical Mg distribution for edge-sorbed Lu would imply a spherical Si distribution, contrary to observations. The alternate interpretation is to assume Lu−Mg pairs oriented at the magic angle (~54.7°) with respect to the normal of the clay layer (the apparent contribution of a shell is invariant at this angle (*11*)). Lu may be located out of the hectorite platelet median plane, close to the extension of the tetrahedral layer. This description would also be consistent with the preferential in-plane orientation of the Si shell.

In the simplest hypothesis, Lu polyhedra bind the hectorite surface via short Lu−O bonds (R_{Lu-O1} = 2.19(2) Å) and share O−O edges with Mg octahedra (R_{Mg-O} = 2.08 Å (*35*)) and corners with Si tetrahedra (R_{Si-O} = 1.62 Å (*38*)). The EXAFS-derived Lu−Mg distance may thus be obtained by summing up the distances from Mg and from Lu to the middle of the shared edge (R_{O-O} = 2.84 Å): R_{Lu-Mg} = 1.52 + 1.67 = 3.19 Å. This value is very close to the experimental distance (3.16(2) Å) and agrees with the distance reported for Y forming inner-sphere surface complexes at the hectorite layer edges (3.16 Å) (*10*). By reference to the local environment of Y-sorbed hectorite, the intermediate Lu−Si distance ($R_{Lu-Mg/Si2}$ = 3.33(1) Å) may be attributed to corner sharing between Si tetrahedra and Lu adsorbed at Mg octahedra edges. Finally, R_{Lu-Si3} = 3.95(2) Å may correspond either to distant Si shells from the hectorite surface, or to Lu polyhedra binding to silanol groups of the tetrahedral sheet in a Lu−O−Si linear geometry, leading to $R_{Lu-Si} \approx R_{Si-O} + R_{Lu-O}$ = 1.62 + 2.33 = 3.95 Å.

Implication for the Fate of Lanthanides in Clay Minerals. Our results show that Lu incorporation in clay octahedral sites is possible, as anticipated from Pauling's empirical rules based on crystal chemistry (*39*), but would result in large strain. The low $N_{Mg/Si1}$ and $N_{Mg/Si2}$ angular dependences suggest that Lu incorporation in hectorite (Lu755Hec) is achieved at the expense of the structure, which may be highly distorted. Consequently, it is anticipated that such a substitution would be even more difficult for larger cations, i.e., with lighter lanthanides and actinides. According to Miller et al. (*36, 37*), the incorporation into clay octahedral sheet is possible for the large Yb(III) (r^{VI}(Yb(III)) = 0.87 Å (*4*)), Ho(III)

(r^{VI}(Ho(III)) = 0.90 Å (*4*)), and Eu(III). However, their diffusion from the interlayer oxygen surfaces, upon ion exchange, to octahedral vacant holes, upon heat treatment, is very limited owing to the high hydration energies of these cations.

Based on crystal chemistry (*39*), lighter lanthanides and actinides may be incorporated in the clay octahedral sheet, but the substitution may be very limited (*36, 37*). However, it can be guessed that the clay mineral may not effectively crystallize in the co-precipitated RN vicinity. Instead, a localized clay-like precipitate may very likely form as a consequence of the high local structural deformation. Nevertheless, such domains would be randomly distributed in the bulk clay structure and have little impact on the clay formation or crystallinity. Such co-precipitates would lead to effective long-term RN immobilization.

Acknowledgments

The European Synchrotron Radiation Facility is acknowledged for provision of synchrotron radiation beamtime. O. Proux and D. Testemale are thanked for their assistance during EXAFS measurements on the FAME (BM30B) beamline. N.F. acknowledges the financial support of the Actinet Network of Excellence.

Supporting Information Available

Figure S1, ATR-FTIR spectra collected for the samples used to prepare self-standing films; Figure S2, XRD patterns of Lu755Hec and Lu/brucite with their assignments; Figure S3, Fourier-filtered EXAFS spectra of the second FT peak of Lu/brucite and Lu/SHCa1, and the broad feature of Lu755Hec; Figure S4, best fit models for the Lu/brucite, Lu755Hec, and Lu/SHCa1 at $\alpha = 10$ and 80°. This material is available free of charge via the Internet at http://pubs.acs.org.

Literature Cited

(1) Abdelouas, A.; Crovisier, J. L.; Lutze, W.; Grambow, B.; Dran, J. C.; Müller, R. Surface layers on a borosilicate nuclear waste glass corroded in $MgCl_2$ solution. *J. Nucl. Mater.* **1997**, *240* (2), 100–111.

(2) Zwicky, H. U.; Grambow, B.; Magrabi, C.; Aerne, E. T.; Bradley, R.; Barnes, B.; Graber, T.; Mohos, M.; Werme, L. O. Corrosion behavior of British Magnox waste glass in pure water. *Mater. Res. Soc. Symp. Proc.* **1989**, *127*, 129–136.

(3) Kim, J. I.; Grambow, B. Geochemical assessement of actinide isolation in a German salt repository environment. *Eng. Geol.* **1999**, *52*, 221–230.

(4) Shannon, R. D. Revised effective ionic radii and systematic studies of interatomic distances in halides and chalcogenides. *Acta Crystallogr.* **1976**, *A 32*, 751–767.

(5) Chapman, N. A.; Smellie, J. A. T. Introduction and summary of the workshop: natural analogues to the conditions around a final repository for high-level radioactive waste. *Chem. Geol.* **1986**, *55*, 167–173.

(6) Allan, N. L.; Blundy, J. D.; Purton, J. A.; Lavrentiev, M. Y.; Wood, B. J. Trace element incorporation in minerals and melts. In *EMU Notes in Mineralogy, Vol. 3: Solid Solutions in Silicates and Oxides Systems*; Geiger, C. A., Ed.; Eötvös University Press: Budapest, 2001.

(7) Spagnuolo, M.; Martinez, C. E.; Jacobson, A. R.; Baveye, P.; McBride, M. B.; Newton, J. Coprecipitation of trace metal ions during the synthesis of hectorite. *Appl. Clay Sci.* **2004**, *27* (3−4), 129–140.

(8) Finck, N.; Stumpf, T.; Walther, C.; Bosbach, D. TRLFS characterization of Eu(III)-doped synthetic organo-hectorite. *J. Contam. Hydrol.* **2008**, *102* (2−3), 253–262.

(9) Brandt, H.; Bosbach, D.; Panak, P. J.; Fanghänel, T. Structural incorporation of Cm(III) in trioctahedral smectite hectorite: A time-resolved laser fluorescence spectroscopy (TRLFS) study. *Geochim. Cosmochim. Acta* **2007**, *71* (1), 145–154.

(10) Schlegel, M. L. Polarized EXAFS characterization of the sorption mechanism of yttrium on hectorite. *Radiochim. Acta* **2008**, *96* (9−11), 667–672.

(11) Manceau, A.; Chateigner, D.; Gates, W. P. Polarized EXAFS, distance-valence least-squares modeling (DVLS) and quantitative texture analysis approaches to the structural refinement of Garfield nontronite. *Phys. Chem. Miner.* **1998**, *25* (5), 347–365.

(12) Carrado, K. A.; Thiyagarajan, P.; Song, K. A study of organo-clay crystallization. *Clay Miner.* **1997**, *32* (1), 29–40.

(13) Schlegel, M. L.; Manceau, A.; Chateigner, D.; Charlet, L. Sorption of metal ions on clay minerals. I. Polarized EXAFS evidence for the adsorption of Co on the edges of hectorite particles. *J. Colloids Interface Sci.* **1999**, *215* (1), 140–158.

(14) López-González, H.; Jiménez-Reyez, M.; Solache-Ríos, M.; Rojas-Hernández, A. Solubility and hydrolysis of lutetium at different $[Lu^{3+}]_{initial}$. *J. Radioanal. Nucl. Chem.* **2007**, *274* (1), 103–108.

(15) Mullica, D. F.; Milligan, W. O. Structural refinement of cubic $Lu(OH)_3$. *J. Inorg. Nucl. Chem.* **1980**, *42* (2), 223–227.

(16) Proux, O.; Nassif, V.; Prat, A.; Ulrich, O.; Lahera, E.; Biquard, X.; Menthonnex, J.-J.; Hazemann, J.-L. Feedback system of a liquid-nitrogen-cooled double-crystal monochromator: design and performances. *J. Synchrotron Radiat.* **2006**, *13* (1), 59–68.

(17) Ravel, B.; Newville, M. ATHENA, ARTHEMIS, HEPHAESTUS: data analysis for X-ray absorption spectroscopy using IFEFFIT. *J. Synchrotron Radiat.* **2005**, *12* (4), 537–541.

(18) Teo, B. K. *EXAFS: Basic Principles and Data Analysis*; Springer Verlag: Berlin, 1986.

(19) Ankudinov, L. A.; Ravel, B.; Rehr, J. J.; Conradson, S. D. Real-space multiple-scattering calculation and interpretation of X-ray-absorption near-edge structure. *Phys. Rev.* **1998**, *B 58* (12), 7565–7576.

(20) Dardenne, K.; Schäfer, T.; Denecke, M. A.; Rothe, J.; Kim, J. I. Identification and characterization of sorbed lutetium species on 2-line ferrihydrite by sorption data modeling, TRLFS and EXAFS. *Radiochim. Acta* **2001**, *89* (7), 469–479.

(21) Allen, P. G.; Bucher, J. J.; Shuh, D. K.; Edelstein, N. M.; Craig, I. Coordination chemistry of trivalent lanthanide and actinide ions in dilute and concentrated chloride solutions. *Inorg. Chem.* **2000**, *39* (3), 595–601.

(22) Schlegel, M. L.; Manceau, A. Evidence for the nucleation and epitaxial growth of Zn phyllosilicate on montmorillonite. *Geochim. Cosmochim. Acta* **2006**, *70* (4), 901–917.

(23) Frost, R. L.; Kloprogge, T. J. Infrared emission spectroscopic study of brucite. *Spectrochim. Acta* **1999**, *A 55* (11), 2195–2205.

(24) Madejovà, J.; Komadel, P. Baseline studies of the Clay Minerals Society source clays: infrared methods. *Clays Clay Miner.* **2001**, *49* (5), 410–432.

(25) Farmer, V. C. *The Infrared Spectra of Minerals*; Mineralogical Society: London, 1974.

(26) Nagai, T.; Hattori, T.; Yamanaka, T. Compression mechanism of brucite: An investigation by structural refinement under pressure. *Am. Mineral.* **2000**, *85* (5−6), 760–764.

(27) Brindley, G. W.; Brown, G. *Crystal Structures of Clay Minerals and their X-ray Identification*; Mineralogical Society: London, 1980.

(28) Yamaguchi, T.; Nomura, M.; Wakita, M.; Ohtaki, H. An extended X-ray absorption fine structure study of aqueous rare earth perchlorate solutions in liquid and glassy states. *J. Chem. Phys.* **1988**, *89* (8), 5153–5159.

(29) Ellison, A. J. G.; Loon, C.-K.; Wagner, J. Neutron scattering studies of Yb-bearing silicate glasses. *J. Alloys Compd.* **1994**, *207−208*, 170–173.

(30) Marcus, M. A.; Polman, A. Local structure around Er in silica and sodium silicate glasses. *J. Non-Cryst. Solids* **1991**, *136* (3), 260–265.

(31) Wilding, M.; Badyal, Y.; Navrotsky, A. The local environment of trivalent lanthanide ions in sodium silicate glasses. A neutron diffraction study using isotopic substitution. *J. Non-Cryst. Solids* **2007**, *353* (52−54), 4792–4800.

(32) Liu, G. K.; Zhorin, V. V.; Antonio, M. R.; Li, S. T.; Williams, C. W.; Soderholm, L. Studies of Cm^{3+} in borosilicate glass using laser and x-ray spectroscopic methods and computational modeling. *J. Chem. Phys.* **2000**, *112* (3), 1489–1496.

(33) Stumpf, T.; Curtius, H.; Walther, C.; Dardenne, K.; Ufer, F.; Fanghänel, T. Incorporation of Eu(III) into hydrotalcite: a TRLFS and EXAFS study. *Environ. Sci. Technol.* **2007**, *41* (9), 3186–3191.

(34) Zigan, T.; Rothbauer, R. Neutronenbeugungsmessungen am Brucit. *Jahrb. Mineral. Monatsh.* **1967**, 137–143.

(35) Seidl, W.; Breu, J. Single crystal structure refinement of tetramethylammonium hectorite. *Z. Kristallogr.* **2005**, *220* (2−3), 169–176.

(36) Miller, S. E.; Heath, G. R.; Gonzalez, R. D. Effect of temperature on the sorption of lanthanides by montmorillonite. *Clays Clay Miner.* **1982**, *30* (2), 111–122.

(37) Miller, S. E.; Heath, G. R.; Gonzalez, R. D. Effect on pressure on the sorption of Yb by montmorillonite. *Clays Clay Miner.* **1983**, *31* (1), 17–21.

(38) Meunier, A. *Clays*; Springer: Berlin, 2005.

(39) Pauling, L. The principles determining the structure of complex ionic crystals. *J. Am. Chem. Soc.* **1929**, *51* (4), 1010–1026.

ES901940V